

Observations of Surface Gravity Wave Spectra from Moving Platforms

LUKE COLOSI^a, NICK PIZZO,^a LAURENT GRARE,^a NICK STATOM,^a AND LUC LENAIN^a

^a Scripps Institution of Oceanography, University of California, San Diego, La Jolla, California

(Manuscript received 22 February 2023, in final form 5 July 2023, accepted 17 July 2023)

ABSTRACT: Surface waves play an important role in the ocean–atmosphere coupled climate system by mediating the exchange of momentum, heat, and gas between the atmosphere and the ocean. Pseudo-Lagrangian autonomous platforms (e.g., Boeing Liquid Robotics Wave Gliders) have been used to investigate the underlying physical dynamics involved in these processes to better parameterize the air–sea exchange occurring at the scale of the surface waves. This requires accurate measurements of directional surface waves down to short scales [$O(1)$ m], as these shorter waves support most of the stress between the atmosphere and the ocean. A challenge to overcome for pseudo-Lagrangian autonomous vehicles is that the platform’s velocity causes the observed frequency of the waves to be Doppler shifted. This leads to a modulation of the wave spectrum, particularly at high frequencies, that depends on the platform’s speed, the wave frequency, and the relative angle between the direction of wave and platform propagation. In this work, we propose a method to account for Doppler effects that considers the full directionality of the wave field. The method is validated using a unique dataset collected from a fleet of two Wave Gliders off the coast of Southern California in September 2019 operating on the perimeter of a tight square (500-m edge length) track over a 3-day deployment. This technique can be used to estimate wave spectra derived from other slow-moving surface vehicles such as Saildrones that use platform motion to characterize the surface wave field. MATLAB routines to implement this method are publicly available.

SIGNIFICANCE STATEMENT: The purpose of this study is to introduce a general approach that corrects observations of ocean surface waves collected on board autonomous surface vehicles (ASVs) for the effects on the wave period due to the vehicle’s forward motion. This is important because improving climate models requires accurate measurements of short-wavelength waves, which can be readily obtained from ASVs. Our method provides the tools for ASVs to better understand air–sea physics and the larger role ocean surface waves play in Earth’s climate system.

KEYWORDS: Ocean; Atmosphere-ocean interaction; Wave properties; Wind waves; In situ oceanic observations; Oceanic waves


1. Introduction

Ocean surface gravity waves play a crucial role in Earth’s climate system by mediating the exchange of energy, momentum, heat, and gases between the ocean and atmosphere (Cavaleri et al. 2012). This is due in part to the ubiquity and dominance of surface waves at the air–sea interface. Quantifying the influence surface waves have on these exchanges is needed to improve our understanding of the physics driving the ocean–atmosphere system, such as the active two-way coupling between winds, waves, and currents. These improvements in physical understanding will lead to advancements in forecasting Earth’s climate in numerical simulations through physics-driven parameterizations of air–sea processes.

To achieve this, acquiring high-quality measurements of the directional surface wave field, especially down to small scales

$O(1)$ m, where most of the stress between the ocean and atmosphere is supported (Mitsuyasu 1985; Melville 1996), is needed. Autonomous surface vehicles (ASVs) measure the wave spectrum as they move across the ocean surface from the vehicle motion by assuming the platform motion closely follows the sea surface displacement of the surface waves (see, e.g., Lenain and Melville 2014; Thomson et al. 2018; Grare et al. 2021). Despite the limitations of this assumption, for example, the platform’s heave response damping of high-frequency waves [see Thomson et al. (2015) for a related discussion on high-frequency attenuation from biofouling on a wave buoy and (Alvarez 2015) for a discussion on Slocum gliders], ASVs have been shown to collect robust estimates of directional wave measurements and bulk wave statistics (Lenain and Melville 2014; Grare et al. 2021). With the recent advancements in the development of ASVs, surface waves may be observed in remote areas over long-duration deployments. Moreover, measurements taken on board these vehicles span broad spatiotemporal scales. This allows these platforms to capture the space and time evolution of the wave field.

Several theoretical, laboratory, and field studies have demonstrated the variety of ways a moving platform can impact measurements of surface waves (e.g., Kats and Spevak 1980; Longuet-Higgins 1986; McAllister and Van Den Bremer 2019). Here, we focus on the impact of platform motion on the

 Denotes content that is immediately available upon publication as open access.

 Supplemental information related to this paper is available at the Journals Online website: <https://doi.org/10.1175/JTECH-D-23-0022.s1>.

Corresponding author: Luke Colosi, lcolosi@ucsd.edu

DOI: 10.1175/JTECH-D-23-0022.1

© 2023 American Meteorological Society. This published article is licensed under the terms of the default AMS reuse license. For information regarding reuse of this content and general copyright information, consult the AMS Copyright Policy (www.ametsoc.org/PUBSReuseLicenses).

observed period of the waves. Differences in observed wave period exist depending on the reference frame of the observer. Longuet-Higgins (1986) showed for example that for steep waves in deep water, the observed wave period measured by a Lagrangian observer (fluid-particle-following reference frame), and an Eulerian observer (fixed-location reference frame), may differ as much as 38% due to a Doppler shift. Wave-following ASVs measure the wave field from a pseudo-Lagrangian perspective because they do not strictly follow fluid particles due to the dynamic response of the platform to the wave forcing and its mechanical propulsion system. The autonomous platform motion relative to the incoming waves causes the observed frequencies to be Doppler shifted. These Doppler effects impact spectral quantities derived from the time series of platform motion by shifting the power spectral density to higher or lower frequencies depending on the platform's velocity relative to the waves.

To obtain wave spectra independent of the platform motion, a frequency mapping to a reference frame free from Doppler effects is required. Previous studies have explored different approaches to the mapping (Drennan et al. 1994; Hanson et al. 1997; Cifuentes-Lorenzen et al. 2013; Collins et al. 2017; Amador et al. 2022) based on the theoretical work of Kats and Spevak (1980). Frequency spectra, hereafter referred to as the one-dimensional (1D) spectrum, have been mapped assuming a unidirectional wave field (usually using a head-sea wave direction or wave direction derived from the platform's drift direction, wind direction, wave model, buoy measurement, or marine radar measurements; see Hanson et al. 1997; Cifuentes-Lorenzen et al. 2013; Collins et al. 2017) or using a frequency-dependent mean wave direction (computed from the first- and second-order Fourier moments of the directional distribution of wave energy; see Lenain and Melville 2014; Amador et al. 2022). A weakness in these methods is that they ignore the full directionality of the wave field, which may cause the mapping to erroneously project spectral energies into wave directions that are not captured by a mean direction characterization (Amador et al. 2022).

In this study, we present a general mapping method, building upon the work of Drennan et al. (1994), that can be applied to any autonomous surface vehicle to account for Doppler effects. Our approach is validated and tested using unique datasets collected by a fleet of Liquid Robotics instrumented Wave Gliders (Grare et al. 2021). We then compare our method with the approaches used in Hanson et al. (1997), Cifuentes-Lorenzen et al. (2013), and Collins et al. (2017) to demonstrate which best removes Doppler effects due to platform motion which is a key assessment missing in previous studies. In addition, we provide detailed descriptions and open-source software tools for implementing the general mapping method. Note that frequency ambiguities when the platform moves in the direction of wave propagation limit our ability to observe the shortest measurable waves from the platform. Here, we provide physical insight into why and where these ambiguities in frequency occur and guidance on how to select the correct branch of the different solution scenarios.

This paper is structured as follows: The overview of the experiments, including the instrumentation used and the range of

environmental conditions encountered, is given in section 2. In section 3, the theoretical background of the frequency mapping between reference frames, the mapping method of the observed two-dimensional spectrum, and the spectral analysis techniques are presented. Section 4 illustrates and discusses the Doppler effects in the observed wave spectra using data collected by instrumented Wave Gliders. A general method for accounting for these Doppler effects is presented and applied to our particular dataset. Finally, section 5 presents a summary of the conclusions and ends with a reference to the open-source code for implementing this method.

2. Experiments, instrumentation, and environmental conditions

a. Experiments

In this study, observations collected from two experiments are investigated. The first was conducted as part of the ONR Task Force Ocean (TFO) initiative. Observations from two Wave Gliders, referenced as “Planck” and “Stokes,” were collected off the coast of Del Mar, California (see Fig. 1), during a 3-day deployment from 9 to 11 September 2020 (referred hereon as DELMAR2020). The two Wave Gliders moved along two tight square tracks: a large square with a 1000-m edge length and a small square with a 500-m edge length. Here, we focus on data from the small square where Doppler effects on the frequency spectrum are more apparent due to rapid changes in platform heading.

The second experiment was conducted as part of the NASA Submesoscale Ocean Dynamics Experiment (S-MODE) program, a project that aims to determine whether submesoscale ocean dynamics make important contributions to the vertical exchange of physical and biological variables in the upper ocean using a combination of aircraft-based remote sensing, research vessels, and autonomous oceanographic platforms measurements along with numerical modeling (Farrar et al. 2020). The pilot experiment considered here was conducted off the coast of San Francisco, California (see Fig. 2), from 29 October to 4 November 2021 (referred hereon as SMODE2021). In this work, we focus on the observations from one of the Wave Gliders deployed in the experiment, referenced throughout as WHOI43.

b. Instrumentation

Instrumented Boeing Liquid Robotics SV3 Wave Gliders are used to collect ocean and atmospheric observations at the air-sea interface (Grare et al. 2021, see their Fig. 1). Included in the present study are atmospheric measurements from a Vaisala WXT (model 530) mounted ~1 m above the ocean surface that records wind speed and direction among other atmospheric parameters. The wind speed 10 m above the ocean surface is estimated using the modified version of the Charnock relation (Charnock 1955) used in the TOGA COARE model (Fairall et al. 2003). Surface wave observations are derived from the motion of the platform (Lenain and Melville 2014; Thomson et al. 2018; Grare et al. 2021) measured by a coupled GPS-inertial motion unit (IMU) system (Novatel SPAN OEM7720-Epson

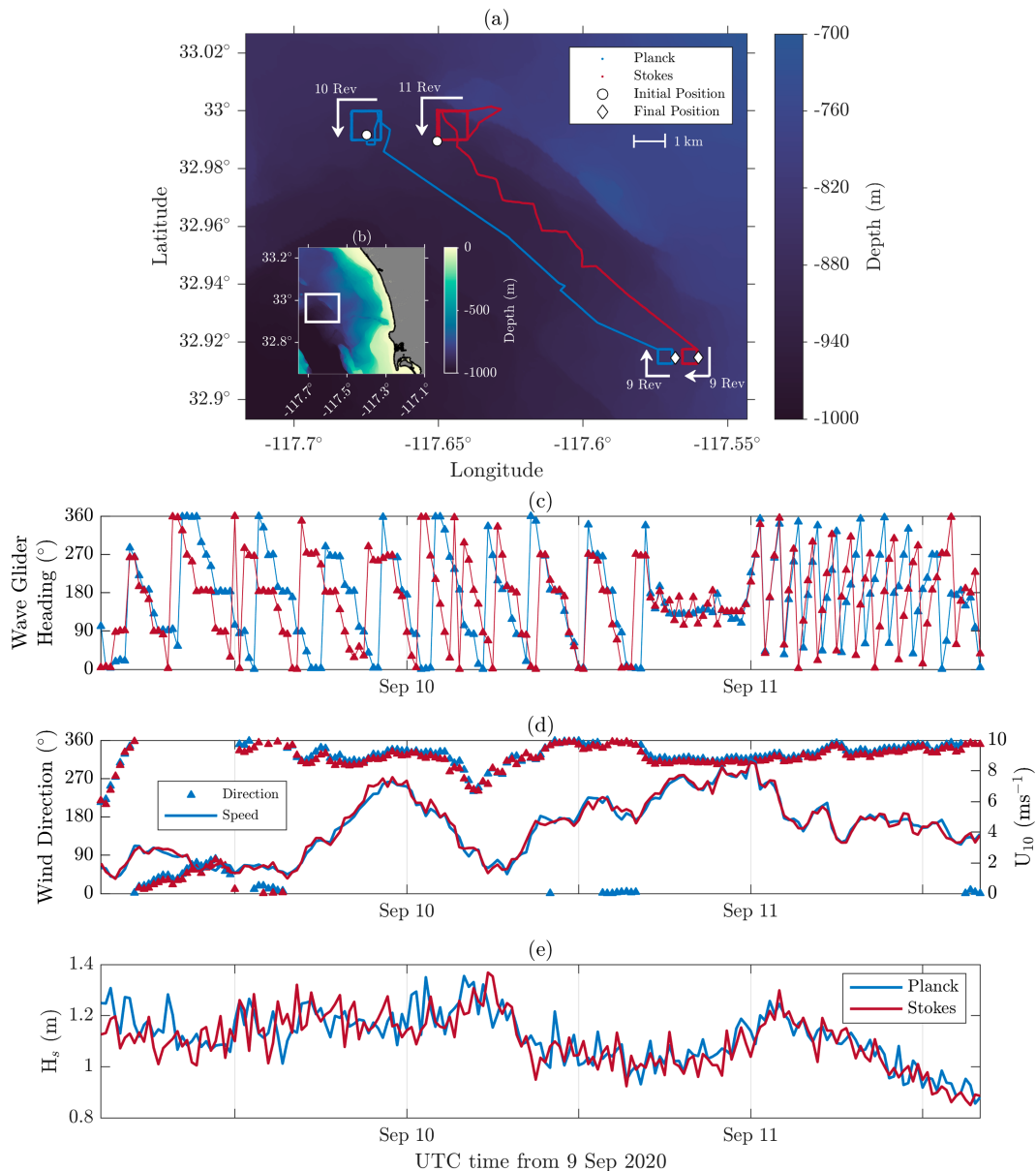


FIG. 1. (a) Trajectories of Wave Gliders Planck (blue) and Stokes (red) during the DELMAR2020 experiment for the time period of 0230 UTC 9 Sep–1610 UTC 11 Sep 2020. (b) The geographic region with the location of the experiment site (white box). (c) Mean platform heading, (d) wind speed at 10 m above the ocean surface (solid line) and wind direction at 1 m above the ocean surface (triangular markers), and (e) significant wave height measured by Planck (blue) and Stokes (red). Here, the directional convention is clockwise, reference north, and going toward.

EG320N for the DELMAR2020 experiment and a Vectornav VN-300 GPS/IMU for the SMODE2021 experiment) (Hodges et al. 2023). Uncertainties in these observations measured by Wave Gliders are discussed in detail by Grare et al. (2021), Thomson et al. (2018), and Lenain and Melville (2014). In these studies, wind and wave observations have been shown to agree well with independent ground truth data over a range of environmental conditions thus demonstrating the high accuracy and precision of these measurements.

c. Environmental conditions

Environmental conditions for the DELMAR2020 and SMODE2021 experiments are shown in Figs. 1d, 1e, 2d, and 2e. During the DELMAR2020 experiment, the sea state was moderate, with 0.8 to 1.4 m significant wave height and variable winds from 1 to 9 m s⁻¹ generally coming from the north-northwest. During the SMODE2021 experiment, significant wave height ranged from 1.5 to 4.5 m and wind speed varied from 1 to 11 m s⁻¹, coming from the northwest at the beginning of the

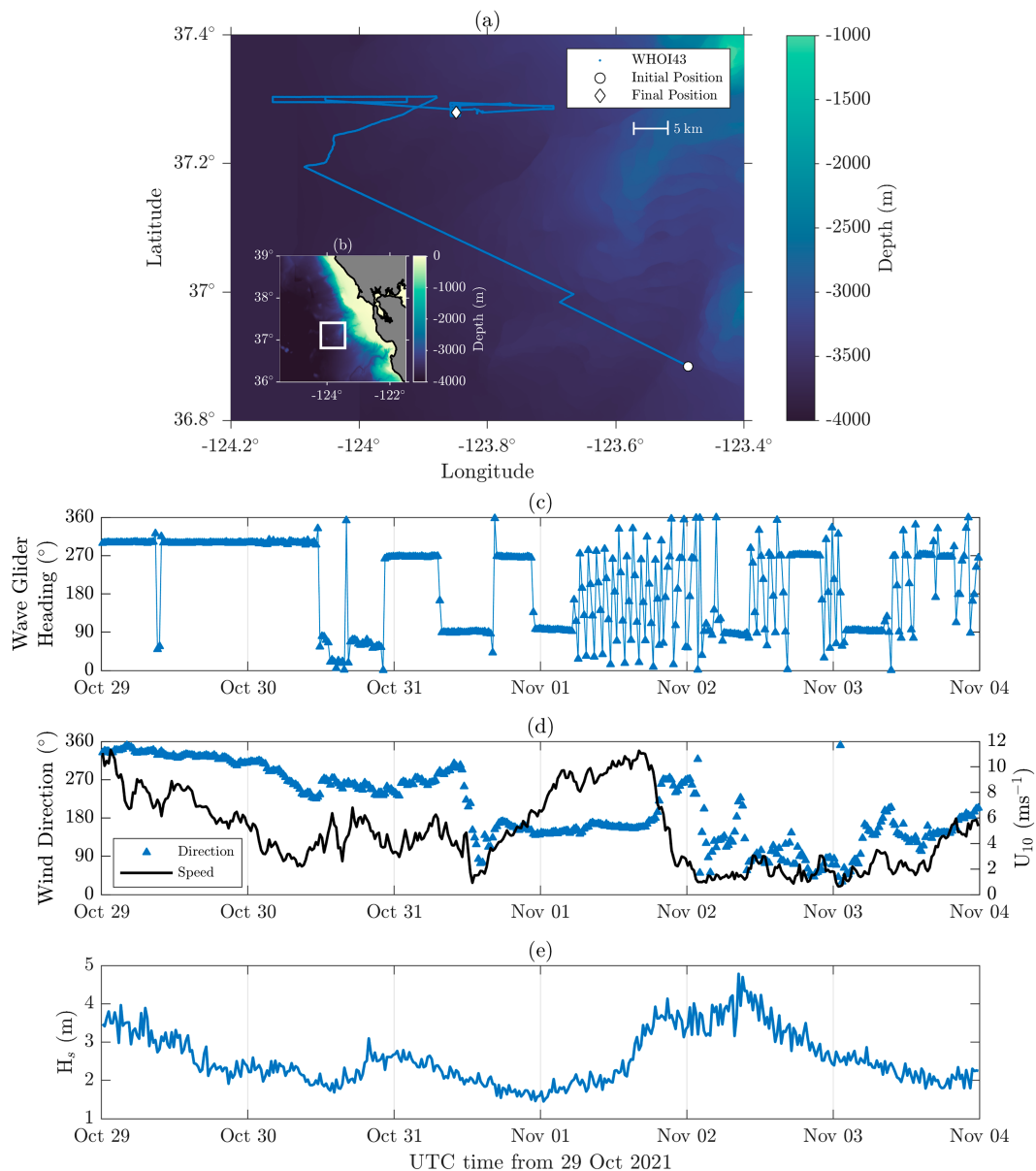


FIG. 2. (a) Trajectory of Wave Glider WHOI43 (blue) during the SMODE2021 experiment for the time period of 0000 UTC 29 Oct–2300 UTC 3 Nov 2021. (b) The geographic region with the location of the experiment site (white box). (c) Mean platform heading, (d) wind speed at 10 m above the ocean surface (solid line) and wind direction at 1 m above the ocean surface (triangular markers), and (e) significant wave height measured by WHOI43 (blue). Here, the directional convention is clockwise, reference north, and going toward.

experiment and shifting toward the south for the rest of experiment. Data from both experiments are investigated to increase the range of environmental conditions.

3. Methods

a. Mapping from observed to intrinsic frequency

Consider two reference frames, R' and R , from which a platform may observe the surface wave field. In R' , the reference frame moves with the platform at a constant velocity \mathbf{u} . In R ,

the reference frame is stationary. Waves measured by the moving observer in reference frame R' are subject to a Doppler shift of their frequencies. That is when the observer is moving against the waves (i.e., in the opposite direction of wave propagation), the observer passes more wave crests in a unit of time compared to a stationary observer, leading to a higher observed frequency or a lower observed wave period. On the other hand, when the observer is moving with the waves (i.e., in the direction of wave propagation), the observer passes fewer wave crests leading to a lower observed frequency or a higher observed wave period.

Waves measured by the stationary observer in reference frame R are free of platform-induced Doppler shifts because the observer velocity relative to the direction of wave propagation vanishes. In contrast to the reference frame dependence of the frequency, the wavenumber vector is invariant between reference frames. Note that this Doppler effect is opposite from the Doppler shift that arises when waves ride upon currents (Peregrine 1976). In the reference frame of a stationary observer, waves advected by a current with uniform velocity are subject to a Doppler shift. For a moving platform, it is the reference frame moving with the platform that experiences a Doppler shift in frequencies.

The cyclical frequency measured on board the stationary platform in reference frame R is the intrinsic frequency f_{in} . The intrinsic frequency is related to the wavenumber magnitude k through the dispersion relation. In this study, the dispersion relationship for deep-water linear surface waves is used:

$$f_{\text{in}} = \frac{\sqrt{gk}}{2\pi}, \quad (1)$$

where g is acceleration due to gravity and $k = |\mathbf{k}|$ with \mathbf{k} being the wavenumber vector. For a platform moving at constant velocity \mathbf{u} in reference frame R' , the cyclical frequency measured on board the vehicle is the observed frequency f_{ob} and is expressed as

$$f_{\text{ob}} = f_{\text{in}}(k) - \frac{\mathbf{k} \cdot \tilde{\mathbf{c}}}{2\pi} = f_{\text{in}}(k) - \frac{kU \cos(\theta_r)}{2\pi}, \quad (2)$$

where $\tilde{\mathbf{c}}$ is the Doppler shift velocity due to the forward platform motion, $U = |\mathbf{u}|$ is the speed platform over ground, and θ_r is the relative direction of platform propagation with respect to the waves. Here, we assume that the currents are slowly varying in time such that over relatively small time scales, the change in wave frequency due to Doppler effects from currents is small compared to the modulations due to changes in the platform's velocity (Bretherton and Garrett 1968). Therefore, there will be a (not necessarily small) *constant* Doppler shift, but here we focus on the relatively short time scale modulations due to the platform's forward motion. We define θ_r using the “coming from” convention as the angle between the direction of a wave component $\theta(\mathbf{k})$, and the direction of platform propagation ϕ , such that

$$\theta_r \stackrel{\text{def}}{=} \theta(\mathbf{k}) - \phi. \quad (3)$$

We set $\theta_r = 0^\circ$ and 180° to be following and head seas, respectively. In these cases, Eq. (2) states that the Doppler shift velocity $\tilde{\mathbf{c}}$ is equal to the velocity of the platform. Properly defining and estimating the Doppler shift velocity is crucial for removing Doppler effects because it sets the magnitude of the Doppler shift term in (2). More details and further discussion are provided in section 3b.

Equation (2) shows that the observed frequency is influenced by the relative motion of the platform with respect to the waves due to its dependence on U and θ_r . Obtaining observations of spectral quantities free from Doppler effects requires a mapping from observed frequency in R' to intrinsic

frequency in R . More specifically, we need to define intrinsic frequency in terms of f_{ob} , U , and θ_r such that $f_{\text{in}}(f_{\text{ob}}, U, \theta_r)$. Note that these inputs are all measurable quantities on board a moving platform. By rearranging (2), we obtain

$$f_{\text{in}}(k, f_{\text{ob}}, U, \theta_r) = f_{\text{ob}} + \frac{kU \cos(\theta_r)}{2\pi}. \quad (4)$$

To write (4) in terms of measurable quantities on board a moving platform, we substitute (1) into (2),

$$2\pi f_{\text{ob}} = \sqrt{gk} - kU \cos(\theta_r), \quad (5)$$

and solve (5) for $k(f_{\text{ob}}, U, \theta_r)$. Rearranging (5) into the form of a quadratic equation with respect to k and solving, we obtain

$$k = \frac{g - 4\pi f_{\text{ob}} U \cos(\theta_r) \pm \sqrt{g^2 - 8\pi f_{\text{ob}} g U \cos(\theta_r)}}{2U^2 \cos^2(\theta_r)}. \quad (6)$$

Substituting (6) into (4), we obtain the desired function:

$$f_{\text{in}}(f_{\text{ob}}, U, \theta_r) = \frac{g \pm \sqrt{g^2 - 8\pi f_{\text{ob}} g U \cos(\theta_r)}}{4\pi U \cos(\theta_r)}. \quad (7)$$

Notice that in (6), multiple solutions for k exist. Together with the solution for k in the absence of platform forward motion which complies with (1),

$$k = \frac{4\pi^2 f_{\text{ob}}^2}{g}, \quad (8)$$

we obtain the complete set of solutions to (5) for any given f_{ob} , θ_r , and U . The physical scenario for each k solution are discussed by Peregrine (1976), Hanson et al. (1997), and Collins et al. (2017). Building upon their work, Table 1 displays the possible k solutions along with the range of θ_r and $U \cos(\theta_r)$ values and a physical description associated with each solution. The term $U \cos(\theta_r)$ represents the platform speed projected onto the wave direction. Variables c and c_g are the phase and group speed, which correspond to the propagation speeds of the wave crests and wave energy, respectively. Both are computed in the R reference frame using the deep water assumption. The term “waves” in the physical scenario column in Table 1 refers to the wave crests. When considering their energy, k_{lt} correspond to waves with energy propagating faster than the projected speed of the platform, while k_{st} and k_r correspond to waves with energy propagation slower than the platform. k_{st} is in a unique situation where the platform speed lies between the energy and crest propagation speeds. See the appendix for further discussion.

Using the five solutions from Table 1, Fig. 3 displays the solutions of Eq. (7) for three cases of platform speed: $U = 0.5, 1$, and 2 m s^{-1} , each with θ_r ranging from 0° (platform moving with waves) to 180° (platform moving against waves).

When the platform moves against the waves for $90^\circ < \theta_r \leq 180^\circ$ (blue-colored curves), f_{ob} is mapped to a lower f_{in} . These observed waves correspond to the solution k_a . A defining characteristic of these curves is their curvature which increases as the platform speed in the direction of wave propagation increases. This

TABLE 1. The k solutions for (5) using variable names from Hanson et al. (1997) in column 1. Columns 2 and 3 specify the form of the solution and the sign in front of the square root, respectively, in (6) and (8). Columns 4 and 5 specify the range of values for the relative direction of platform propagation with respect to the waves and the platform speed projected onto the wave direction; c and c_g are the phase and group speeds, respectively. Column 6 provides a description of the platform-wave system, specifically their speed and direction relative to each other. The phase speed is considered when discussing waves in column 6.

k	Solution	Square root sign	Relative direction domain	Projected speed domain	Physical scenario
k_a	(6)	(-)	$90^\circ < \theta_r < 270^\circ$	$U \cos(\theta_r) < 0$	Approaching waves
k_p	(8)		$\theta_r = 90^\circ, 270^\circ$	$U \cos(\theta_r) = 0$	Waves moving perpendicularly
k_{lt}	(6)	(-)	$0^\circ \leq \theta_r < 90^\circ, 270^\circ < \theta_r \leq 360^\circ$	$0 < U \cos(\theta_r) < c_g$	Long-wavelength overtaking waves
k_{st}	(6)	(+)	$0^\circ \leq \theta_r < 90^\circ, 270^\circ < \theta_r \leq 360^\circ$	$c_g < U \cos(\theta_r) < c$	Short-wavelength overtaking waves
k_r	(6)	(+)	$0^\circ \leq \theta_r < 90^\circ, 270^\circ < \theta_r \leq 360^\circ$	$c < U \cos(\theta_r)$	Overrun waves

curvature reflects the dispersive nature of deep water surface waves. That is, the nonlinearity of (1) causes the slope of (7) to vary with f_{ob} . This can be visualized in Fig. A1 (see appendix for details). Note that in the case of nondispersive waves, the relationship between f_{ob} and f_{in} is linear. This reflects the fact that the slope of the dispersion relation is constant. Due to the downward shift in frequency, the highest resolved frequency in observed frequency space, the observed Nyquist frequency, is reduced to a lower intrinsic Nyquist frequency (Cifuentes-Lorenzen et al. 2013). This places a high-frequency limit on the wave frequencies resolved by a platform moving against the waves.

Turning to $\theta_r = 90^\circ$ (green curve), the platform moves perpendicularly to the waves and the observed frequency is equal to the intrinsic frequency. These waves are represented by the solution k_p . Here, the platform speed in the direction of wave propagation vanishes, indicating the transition between following and head seas as denoted by the dashed black line. Thus, the platform acts as a stationary observer.

Last, when the platform moves with the waves for $0^\circ \leq \theta_r < 90^\circ$ (red-colored curves), f_{ob} is mapped to a higher f_{in} . These waves correspond to three solutions, namely, k_{lt} , k_{st} , and k_r . Solution k_{lt} corresponds to long-wavelength waves whose phase and group speed in R are faster than the platform speed in the direction of wave propagation. In Fig. 3c for $\theta_r = 0$, this solution corresponds to f_{in} values before the inflection point where f_{in} bends back toward lower frequencies. This inflection point is also known as the bifurcation point between k_{lt} and k_{st} . Solution k_{st} corresponds to short-wavelength waves whose phase speed is faster than the platform speed in the direction of wave propagation, but whose group speed is slower. This solution corresponds to f_{in} values after the inflection point but before the zero crossing. Solution k_r corresponds to even shorter-wavelength waves whose phase and group speeds are both slower than the platform speed in the direction of wave propagation. This solution corresponds to f_{in} values after the zero crossing. Note that k_r is obtained using negative observed frequencies in (6).

For $90^\circ \leq \theta_r \leq 180^\circ$, the mapping is bijective such that one observed frequency gets mapped to one unique intrinsic frequency. This is illustrated by the fact that the first derivative of $f_{in}(f_{ob}, U, \theta_r)$ with respect to f_{ob} does not change sign or vanish. However, this is not the case for $0^\circ \leq \theta_r < 90^\circ$. For a range of U and $\theta_r > 90^\circ$, one observed frequency gets mapped to two intrinsic frequencies (e.g., Fig. 3c with $U = 2 \text{ m s}^{-1}$ and $\theta_r = 0^\circ$). Note that when the platform speed in the direction

of wave propagation is sufficiently slow, such as in Fig. 3a, this mapping remains bijective. This is because the observed Nyquist frequency is lower than the bifurcation point between the k_{lt} and k_{st} solutions. The bifurcation point between k_{lt} and k_{st} occurs when the first derivative of $f_{in}(f_{ob}, U, \theta_r)$ with respect to f_{ob} tends toward infinity. Differentiating f_{in} with respect to observed frequency, we obtain

$$\frac{\partial f_{in}}{\partial f_{ob}} = \pm \frac{g}{\sqrt{g^2 - 8\pi f_{ob} g U \cos(\theta_r)}}. \quad (9)$$

Setting the denominator equal to zero and solving for the observed frequency, we obtain the observed frequency at the bifurcation point in intrinsic frequency space:

$$f_{ob} = \frac{g}{8\pi U \cos(\theta_r)}. \quad (10)$$

Substituting (10) into (7), we obtain

$$f_c = \frac{g}{4\pi U \cos(\theta_r)}, \quad (11)$$

the highest intrinsic (cutoff) frequency before the solution bifurcates to the other branch of the solution. By rearranging (11) and using the group speed, given in the R reference frame for deep water surface waves as $c_g = g/(4\pi f_{in})$, (11) becomes

$$U \cos(\theta_r) = c_g. \quad (12)$$

This is consistent with the boundaries of the $U \cos(\theta_r)$ domains for k_{lt} and k_{st} in Table 1. The intrinsic frequency as a function of f_{ob} that satisfies (12) is displayed as the gray dashed lines in Fig. 3 with gray circles corresponding to the cutoff frequencies f_c associated with the given U and θ_r values. See the appendix for more details on the significance of this criterion.

The existence of the cutoff frequency states that the motion of the platform relative to the waves limits the high-frequency waves that a moving platform can observe. That is, when moving in the direction of wave propagation, the platform cannot resolve frequencies above the cutoff frequency (11) which is illustrated in the frequency ambiguity in the mapping (7). Figure 4 shows f_c as a function of U and θ_r (Fig. 4a) along

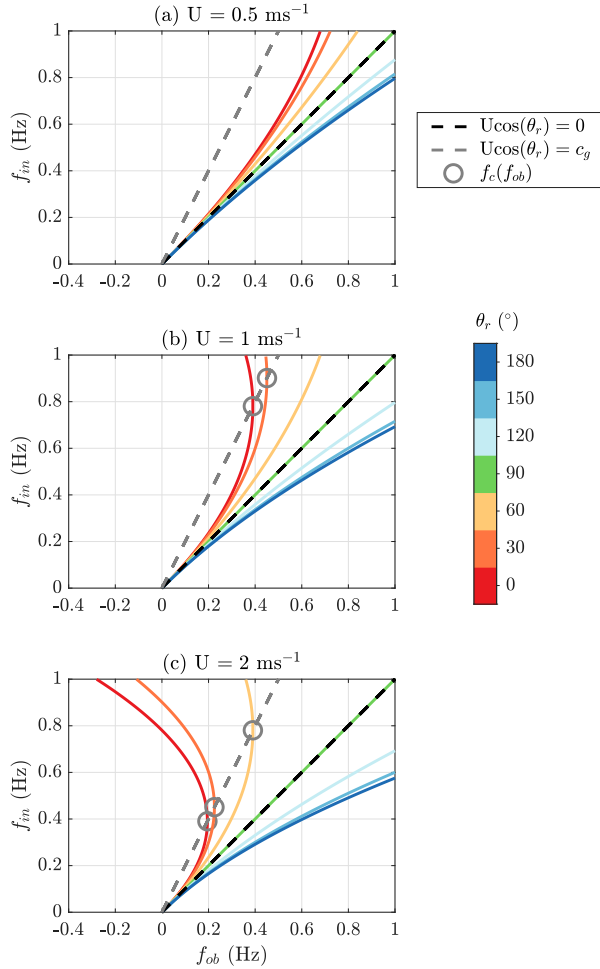


FIG. 3. Mapping from observed to intrinsic frequency for a platform moving at (a) 0.5, (b) 1, and (c) 2 m s⁻¹ with line color corresponding to the platform's direction relative to the waves. The platform moves with the waves when θ_r ranges from $0^\circ \leq \theta_r < 90^\circ$ (red curves) and moves against the waves when θ_r ranges from $90^\circ < \theta_r \leq 180^\circ$ (blue curves). The platform moves perpendicular to the waves when $\theta_r = 90^\circ$. The gray dashed line is the cutoff frequency f_c with intersecting gray circles being f_c for a given direction. The black dashed line is the one-to-one line occurring when the projected speed vanishes ($\theta_r = 90^\circ$).

with a slice of the polar plot for $\theta_r = 0$ (Fig. 4b). It shows that as the measurement platform increases speed and θ_r approaches 0° , the cutoff frequency decreases. For example, at $U = 3 \text{ m s}^{-1}$, the cutoff frequency is as low as 0.26 Hz. Thus, the spectral range reduces considerably and limits the highest-frequency waves that may be measured. The typical speed range for Saildrones (Gentemann et al. 2020), a type of ASV equipped to measure surface waves, extends up to 3 m s^{-1} with an average speed of 1.25 m s^{-1} . Autonauts (Dallolio et al. 2019), another type of ASV, can achieve similar speeds ranging up to 2 m s^{-1} . Careful consideration of the speed and direction of these and other ASVs is recommended during

experimental planning to maximize the highest frequency resolved.

The frequency ambiguity in the case of the following seas presents a dilemma for mapping the 1D and 2D wave spectra. Here, the two-dimensional (2D) spectrum refers to the directional-frequency spectrum. For sufficiently large values of $U \cos(\theta_r)$, we are faced with an ambiguity in determining how to allocate energy from one observed frequency to two intrinsic frequencies. To resolve this, we must choose from one of the two intrinsic frequencies from the mapping, namely, k_{lt} or k_{st} . To do so, we solve (5) using the Newton–Raphson root-finding algorithm (Verbeke and Cools 1995) with an initial guess for k when the platform's velocity vanishes (i.e., $k = k_p$). Using this numerical approach, we find that the k_{lt} solution should be used. See the appendix for more information.

b. A practical 2D method to account for Doppler effects in wave spectra

The methods outlined by Hanson et al. (1997), Cifuentes-Lorenzen et al. (2013), Collins et al. (2017), and Amador et al. (2022), referred to hereafter as the 1D method, start with the observed 1D spectrum $S_{ob}(f_{ob})$. The observed 1D spectrum is obtained by either integrating the observed 2D spectrum over all directions or computing the frequency spectrum of the platform's vertical displacement using the Welch method (Bendat and Piersol 2011). Next, the Doppler shift velocities are computed by finding the mean platform speed \bar{U} and heading $\bar{\phi}$, and the mean wave direction assuming a unidirectional wave field (Hanson et al. 1997; Cifuentes-Lorenzen et al. 2013; Collins et al. 2017) or mixed seas with a wave direction for each frequency resolved in the observed 1D spectrum (Amador et al. 2022). From here, the observed frequency is mapped to intrinsic frequency using the Doppler shift velocity and the Jacobian of the mapping. The Jacobian is defined as df_{ob}/df_{in} . The wave direction is invariant under this mapping as a result of the invariance of the wavenumber vector. Last, the observed 1D spectrum is mapped into the intrinsic frequency space. For the 1D method, we define the intrinsic 1D spectrum as

$$S_{in}(f_{in}) = S_{ob}(f_{ob}) \frac{df_{ob}}{df_{in}}. \quad (13)$$

The general approach presented here following Drennan et al. (1994), referred to hereafter as the 2D method, seeks to improve the 1D method by considering the full directionality of the wave field. To begin, the observed directional wave spectrum $S_{ob}(f_{ob}, \theta)$ is derived from experimental data of platform motion collected on board an ASV (see section 3b for details). Note that the subscript i referenced in the steps below is used to indicate that θ takes on a discrete set of direction values set by the azimuthal resolution of the directional wave spectrum.

Explicitly, the 2D method procedure (Fig. 5) consists of the following steps:

- 1) Compute the observed 2D spectrum $S_{ob}(f_{ob}, \theta)$ and Doppler shift velocity \tilde{c} .

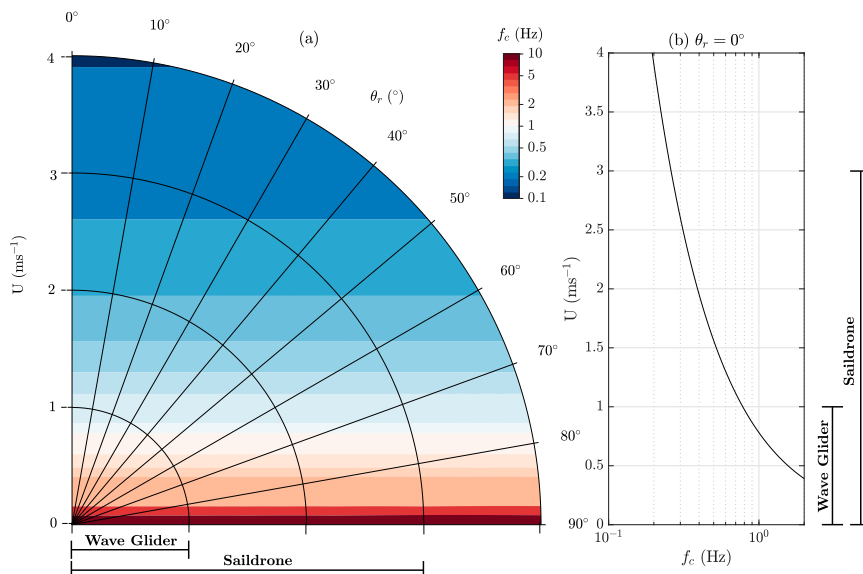


FIG. 4. (a) Cutoff frequency f_c as a function of platform speed and the relative angle between platform heading and wave propagation direction. Relative angles range from 0° to 90° corresponding to the platform moving with the waves. The typical range of speeds for Wave Glider and Saildrone platforms are shown along the radial axis. (b) Cutoff frequency as a function of platform speed for a platform moving strictly in the direction of wave propagation ($\theta_r = 90^\circ$; green curve).

- 2) Project the Doppler shift speed onto the wave direction θ_i . Here, we define this projection as

$$\tilde{c}_p = \bar{U} \cos(\theta_i - \bar{\phi}). \quad (14)$$

- 3) Map from the observed frequency to the intrinsic frequency using the projected speed \tilde{c}_p .
- 4) Compute the Jacobian of the mapping $df_{\text{ob}}/df_{\text{in}}$ using finite differencing.
- 5) Map the observed 2D spectrum in the θ_i direction $S_{\text{ob}}(f_{\text{ob}}, \theta_i)$ into intrinsic frequency space. Here, we define the intrinsic 2D spectrum in the wave direction θ_i as

$$S_{\text{in}}(f_{\text{in}}, \theta_i) = S_{\text{ob}}(f_{\text{ob}}, \theta_i) \frac{df_{\text{ob}}}{df_{\text{in}}}. \quad (15)$$

- 6) Interpolate the intrinsic 2D spectrum in the θ_i direction onto a regular grid.
- 7) Repeat steps 2–6 for each wave direction θ_i in the observed 2D spectrum.
- 8) Compute the intrinsic 1D spectrum $S_{\text{in}}(f_{\text{in}})$ by azimuthally integrating the intrinsic 2D spectrum $S_{\text{in}}(f_{\text{in}}, \theta)$:

$$S_{\text{in}}(f_{\text{in}}) = \int_0^{2\pi} S_{\text{in}}(f_{\text{in}}, \theta) d\theta. \quad (16)$$

The highest frequency resolved in the intrinsic 1D spectrum, defined as f_b , is set by the Nyquist frequency, the bifurcation frequency, the Jacobian, and the interpolation process. This high-frequency cutoff leads to a reduced spectral range. See

online supplementary material for more information. Note, for step 2, the mean speed of the Doppler shift velocity \bar{U} is computed by projecting the platform speed at each time step onto the mean platform heading and averaging these quantities over the time period where the observed 2D spectrum is calculated. The source code to implement the 2D method is published on an open-source platform to facilitate scientific efforts to investigate surface waves down to short spatial scales. For more information, see supplementary material.

c. Spectral analysis

In the following analysis, we investigated the properties of 1D and 2D spectra using data collected from the Wave Gliders deployed in the DELMAR2020 and SMODE2021 experiments. Spectra were computed over the frequency band $0.01 \leq f \leq 1$ Hz. The conservative upper limit of 1 Hz was chosen such that waves with a wavelength less than half the length of the Wave Glider were removed from the analysis. At these high frequencies, the platform's heave response does not represent the true motion of the ocean surface. Here, the observed $S_{\text{ob}}(f_{\text{ob}}, \theta)$ is computed from the vertical displacement and the horizontal velocities measured by the Novatel or Vectrnav inertial navigation sensors using the WAFO toolbox (Brodtkorb et al. 2000) with the maximum entropy method (Lygre and Krogstad 1986), an improvement from the maximum likelihood method used in Drennan et al. (1994). Note, the maximum entropy method provides an estimate of $S_{\text{ob}}(f_{\text{ob}}, \theta)$ using moments of the directional spectrum and assumptions about the directional

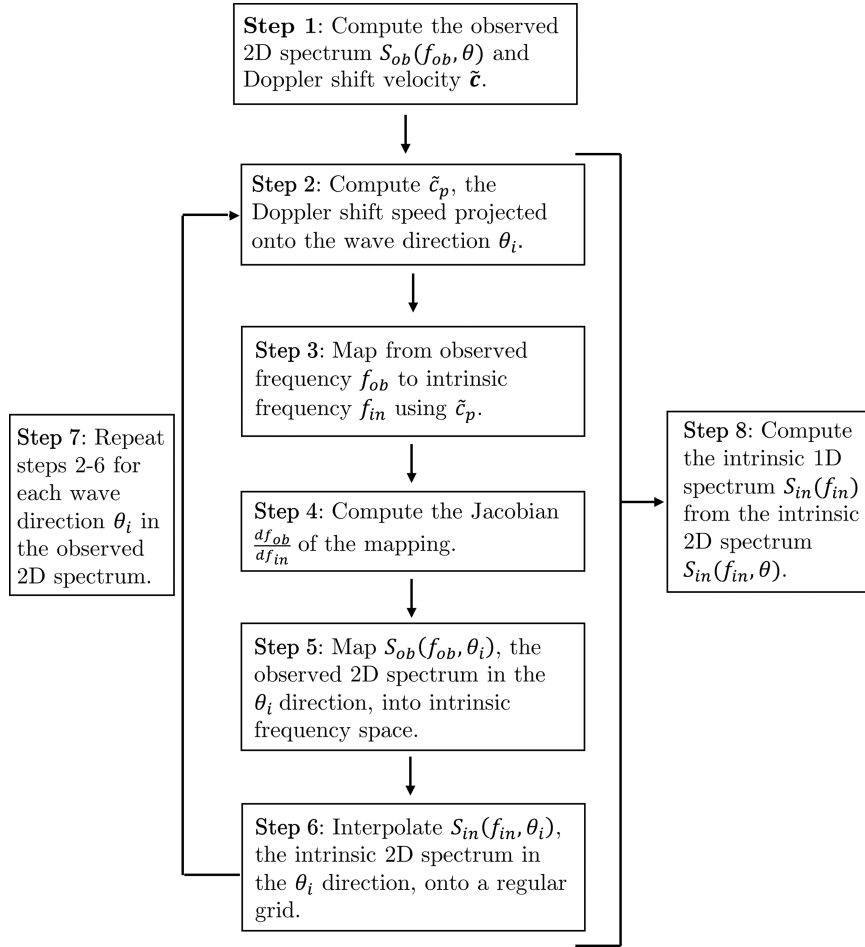


FIG. 5. Flowchart of the 2D method procedure.

spreading. We define the observed 1D spectrum as the azimuthally integrated directional wave spectrum:

$$S_{ob}(f_{ob}) \stackrel{\text{def}}{=} \int_0^{2\pi} S_{ob}(f_{ob}, \theta) d\theta. \quad (17)$$

The observed 1D spectrogram $S_{ob}(t, f_{ob})$ is then obtained by computing observed 1D spectra over consecutive time intervals. To investigate the high-frequency wave band in the 1D spectra, we define the observed saturation spectrum as

$$B_{ob}(f_{ob}) \stackrel{\text{def}}{=} f_{ob}^5 S_{ob}(f_{ob}). \quad (18)$$

In this regime, the Phillips (1985) spectral model predicts a balance between the wind forcing and wave-breaking terms in the statistical equilibrium radiative transfer equation (the nonlinear interaction term becomes negligible in this range due to the short time scales), resulting in an f^{-5} slope in the 1D spectrum. Above the saturation regime lies the equilibrium regime where a three-way balance between wind forcing, dissipation, and nonlinear interactions exists. An f^{-4} slope characterizes

this regime. By multiplying the 1D spectrum by f_{ob}^{-5} , we weigh high-frequency waves over low-frequency waves, allowing investigation of the power spectral density's variability in the high-frequency band.

Figure 6 shows a typical observed directional wave spectrum computed from Wave Glider Stokes during a single leg of the large 1000-m box trajectory in the DELMAR2020 experiment. The directions reported are the directions from which waves are propagating (“coming from” convention). The observed directional spectrum has two large peaks, indicating a local wind sea from the west and a lower-frequency swell from the south. One-dimensional and saturation spectra computed from the directional wave spectra shown in Fig. 6 are plotted in Figs. 7a and 7b, respectively, which further illustrate the presence of mixed-seas conditions with a swell peak of $f_{ob} = 0.07$ Hz and a wind sea peak around $f_{ob} = 0.2$ Hz. Note that the transition frequency between the saturation and equilibrium regimes f_m , shown with the solid vertical line calculated following Lenain and Pizzo (2020), is resolved with f_{ob}^{-4} and f_{ob}^{-5} spectral slopes observed. The 1D and saturation spectrograms for the entire DELMAR2020 experiment are shown in Fig. 8. The time period over which

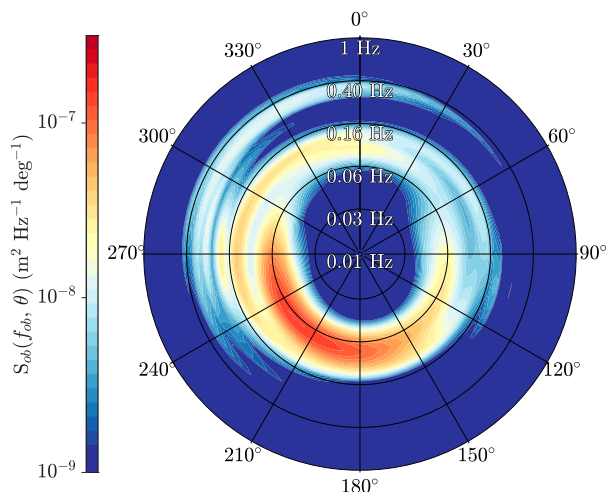


FIG. 6. An observed directional wave spectrum computed from measurements collected on board Wave Glider Stokes during a single fixed heading leg of the large 1000-m box trajectory in the DELMAR2020 experiment (at 2357:06 UTC 9 Sep–0025:18 UTC 10 Sep 2020).

spectra in Figs. 6 and 7 are computed is shown with dot-dashed black vertical lines, while the rectangle enclosed by the dashed line denotes the period of time when the Wave Glider Stokes moved in the small 500-m box formation. Overall, Fig. 8 shows that the wave field was primarily dominated by swells; at the beginning of the experiment, starting separately on 10 and 11 September, two wind-sea wave systems developed, which is consistent with increases in observed wind speed coming from the northwest. Note that the white area at high frequencies around 1200 UTC 9 September 2020 is an artifact of the directional wave spectrum computation. In calm seas, the horizontal velocity and vertical displacement of the vehicle are sometimes insufficient to obtain an

accurate power spectral density estimate at high frequency in certain wave directions (usually in directions with low variance in the wave field). These frequencies are discarded in Fig. 8.

The analysis of spectral quantities discussed above is split into two steps. In step 1, we aim to demonstrate the significant impact Doppler effects have on the saturation spectra, especially at high frequencies. To accomplish this, we focus on the small 500-m box pattern from the DELMAR2020 experiment (Fig. 1a) and compute spectra over time records when the Wave Glider is moving in a constant heading along the legs of the box. By doing so, we isolate the effect that a constant heading has on the spectra. The small box is orientated such that the platform moves almost directly against the waves on the north-to-south legs while it moves with the waves on the south-to-north legs. Note that a single leg of the small box took about 21 min to complete on average, in turn minimizing the natural spatial and temporal variability of the wave field. In the second step, where we aim to characterize the efficiency of the 2D mapping method, the saturation spectrogram is computed over constant time intervals (10-min records) independent of the heading of the platform for the entire experiment.

4. Results

We now examine observations collected from the Wave Glider Stokes during the time period of the DELMAR2020 experiment when it was moving in a tight square box formation. We compute the saturation spectrum for each leg of the small 500-m box formation and exclude measurements when the Wave Glider is turning. Figure 9a shows the time series of the mean propagation direction for Stokes along the legs of the small 500-m box with the marker color denoting whether the Wave Glider moves against or with the mean propagation direction of high-frequency waves $f_{ob} > 0.1$ Hz. Waves within this high-frequency band have a mean wave direction coming from the northwest. Figure 9b is the observed saturation

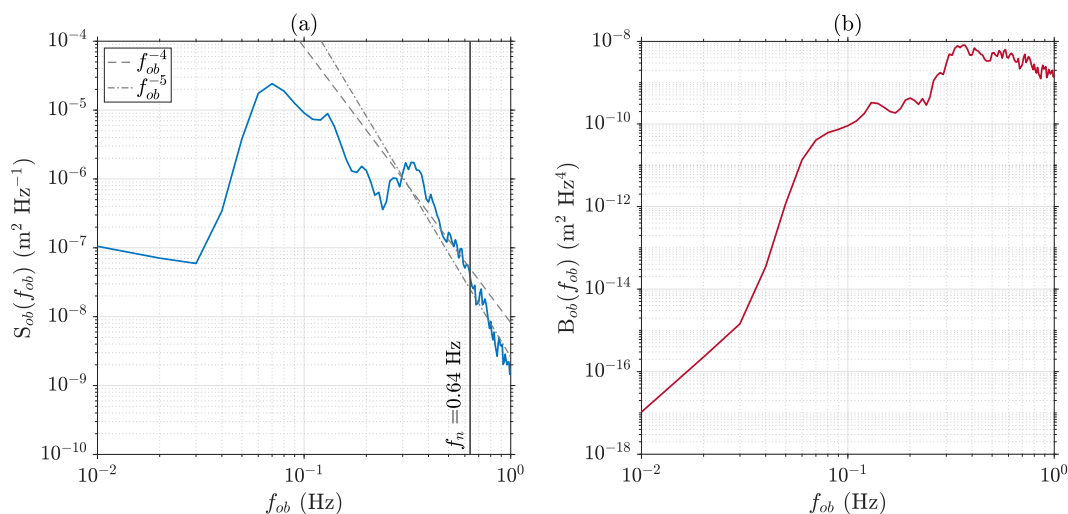


FIG. 7. Observed (a) 1D and (b) saturation spectra computed from the directional wave spectrum in Fig. 6. The dashed and dot-dashed lines have f_{ob}^{-4} and f_{ob}^{-5} spectral slopes, respectively.

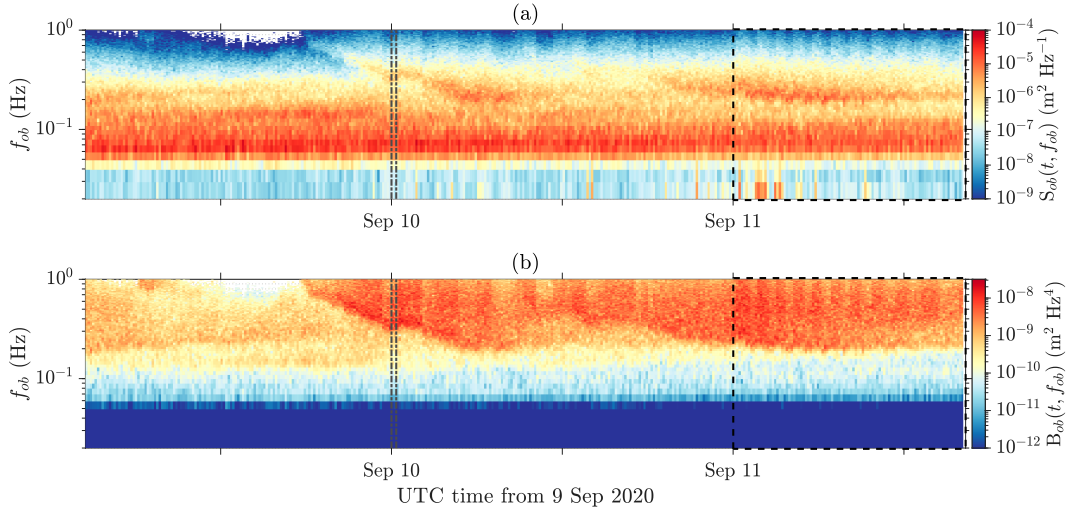


FIG. 8. Observed (a) 1D and (b) saturation spectrograms computed from measurements collected on board the Wave Glider Stokes during the DELMAR2020 experiment. The dot-dashed vertical lines outline the time period from which spectral quantities in Figs. 6 and 7 are derived. The dashed rectangle outlines the time period when the Wave Glider Stokes traversed in its small 500-m box formation (Fig. 1).

spectrogram computed for each leg. We find large fluctuations in the saturation spectrogram spectral levels over time, in particular at high frequencies, i.e., $f_{ob} > 0.1$ Hz, strongly correlated with the change in the projected speed of the Wave Glider in the direction of the mean wave direction $\bar{\theta}$, defined as

$$U_p = \bar{U} \cos(\bar{\theta} - \bar{\phi}), \quad (19)$$

with \bar{U} being the mean projected speed of the Wave Glider in the platform propagation direction as defined previously. Fluctuations are particularly pronounced at frequencies ~ 0.2 Hz where we find rapid changes in saturation spectral levels as a function of time. These fluctuations at high frequencies are somewhat less pronounced due to the noise being amplified by multiplying the 1D spectrum by f_{ob}^{-5} . Figure 9c shows two

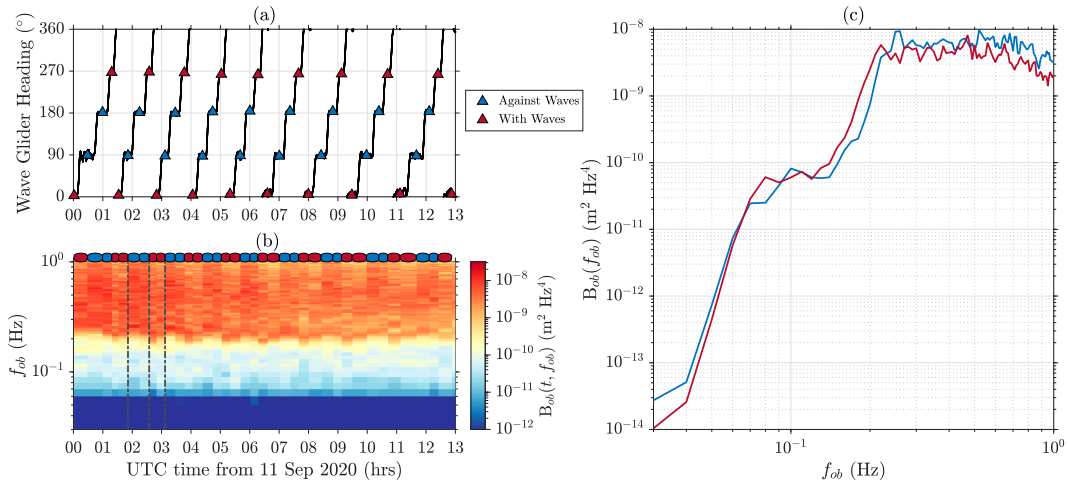


FIG. 9. (a) Wave Glider Stokes's heading (using the coming from directional convention) for the small 500-m box legs. Red triangles denote the legs where the platform is moving in the direction of wave propagation for high-frequency waves ($f_{ob} > 10^{-1}$ Hz). Blue triangles denote the legs where the platform is moving against the direction of wave propagation for high-frequency waves. These high-frequency waves have a mean wave direction coming from the northwest (approximately 300°). (b) Saturation spectrogram for Wave Glider Stokes's repeated small 500-m box formation with red and blue colored ovals along the top axis specifying the relative angle between platform heading and mean wave direction for high-frequency wave using the same color code as in Fig. 9a. Saturation spectra within the two time periods outlined by dot-dashed vertical lines correspond to the averaged spectra in Fig. 9c. (c) Two averaged saturation spectra showing against (red curve) and with (blue curve) wave cases.

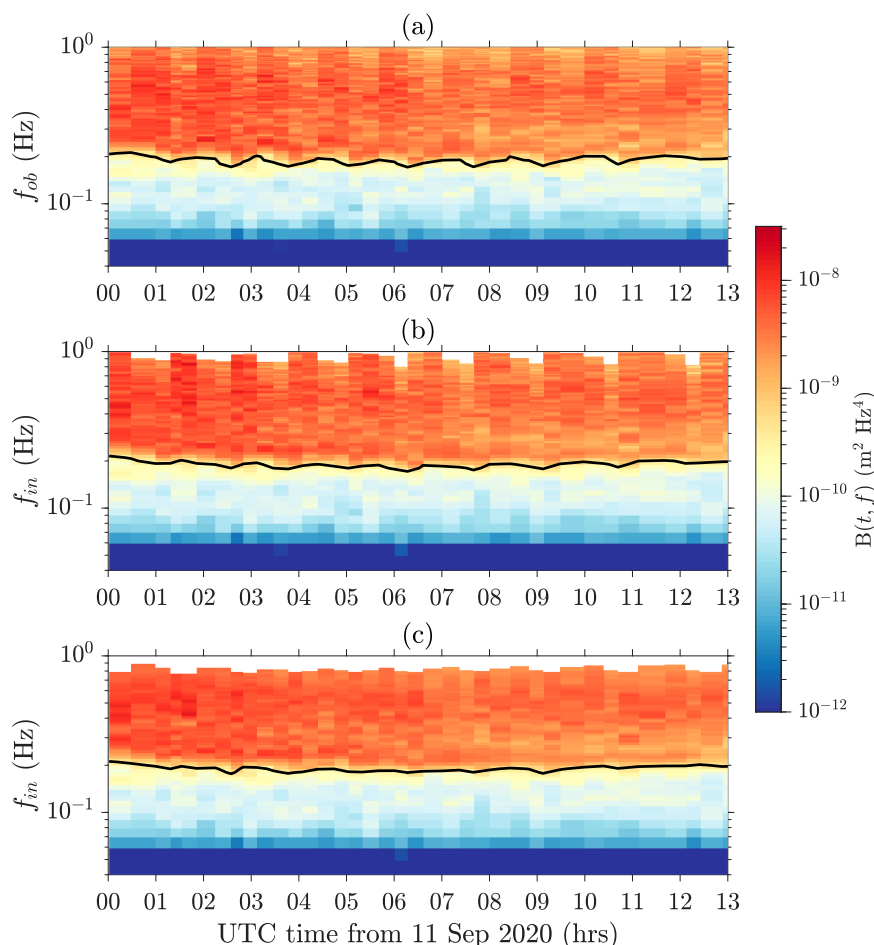


FIG. 10. Saturation spectrogram for Wave Glider Stokes's repeated small 500-m box trajectory in (a) observed frequency space and intrinsic frequency space using the (b) 1D and (c) 2D methods. The black curve is the $6 \times 10^{-10} \text{ m}^2 \text{ Hz}^4$ saturation spectral level contour to emphasize fluctuation.

average saturation spectra computed over legs of different headings, corresponding to the two time periods outlined by dot-dashed vertical lines in Fig. 9. We find that in the against-wave leg, where the observed frequency is shifted to higher frequencies, the saturation spectral level is higher than in the case where the waves and the platform are propagating in the same direction.

Figure 10a shows the same observed saturation spectrogram presented in Fig. 9b along with the Doppler-corrected saturation spectrograms computed using the (Fig. 10b) 1D and (Fig. 10c) 2D methods. Note that the 1D method results assume a unidirectional wave field, taking the mean wind direction as the wave direction. The saturation spectrograms in Figs. 10a and 10b are frequency limited such that the intrinsic frequencies that are greater than f_b are not resolved. We also find that the directional fluctuations in the saturation spectrogram are still present when using the 1D method. Here, this projection leads to the overcompensation of the power spectral density such that the saturation spectral level is mapped to either too high (with-wave legs) or too low (against-wave legs) of levels. In contrast, the 2D method

used in Fig. 10c removes nearly all fluctuations. This is particularly evident in the shape of the contour line of the saturation spectrogram taken at $B = 6 \times 10^{-10} \text{ m}^2 \text{ Hz}^4$ (shown in all panels of Fig. 10). This saturation spectral level was chosen because it is close to the frequency regime where fluctuations are most pronounced.

To quantify this improvement, we compute the correlation coefficient between the time series of the Wave Glider's projected speed in the mean wave direction at high frequency and the mean saturation $\langle B \rangle$ defined here as the average saturation spectral level over the frequency band from 0.1 to 1 Hz in both observed and intrinsic frequency space. The low limit of this frequency band is chosen such that the fluctuations around 0.2 Hz are included in the mean saturation estimate. We find the correlation to be $r = -0.546, 0.407$, and 0.196 for observed, 1D, and 2D methods, respectively. These findings support the argument that the 2D method presented here is the most effective approach to accounting for Doppler effects in 1D spectra. The method correctly projects the spectral energy onto frequencies such that fluctuations in

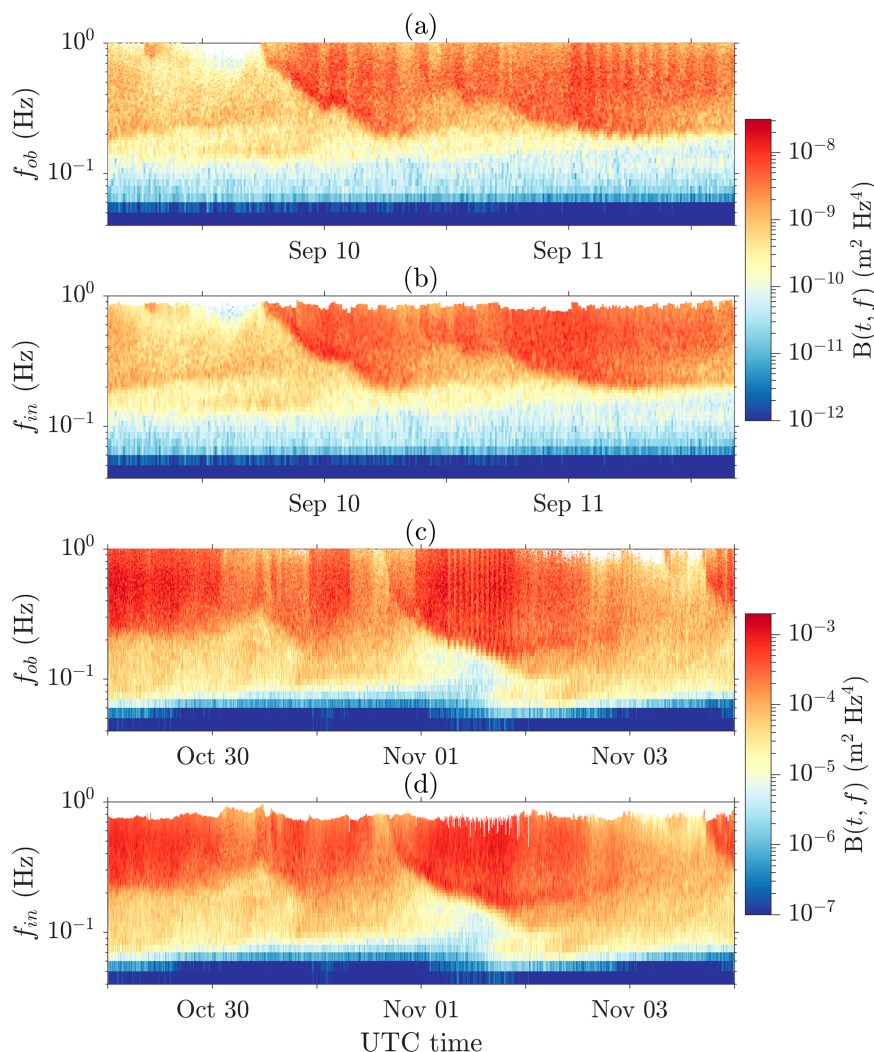


FIG. 11. (a),(c) Observed and (b),(d) intrinsic saturation spectrograms during the (a),(b) DELMAR2020 and (c),(d) SMODE2021 experiments for Wave Gliders (a),(b) Stokes and (c),(d) WHOI43. Spectrograms were computed over 10-min intervals independent of the Wave Glider heading.

power spectral density over time are removed across all frequencies.

Last, we applied the 2D method to the saturation spectrogram computed over 10-min intervals for the entire DELMAR2020 and SMODE2021 experiments independent of platform heading (Fig. 11). Here, only spectrograms from Wave Gliders Stokes and WHOI43 are shown (similar results were found with Wave Glider Planck). We find that the 2D method performs well, removing any spurious fluctuations. Note that the f_b for the SMODE2021 experiment is particularly low, especially from 1 to 2 November (minimum $f_b = 0.5$ Hz). This is due to the high velocity of the platform during this time period (mean platform speed $\bar{U} = 0.76 \pm 0.015$ m s⁻¹ with a maximum peak speed of 1.2 m s⁻¹). Additionally, the 2D method is capable of handling complex seas scenarios (e.g., see from 0000 to 1630 UTC 11 September in Figs. 11a,b).

5. Discussion and summary

Autonomous surface vehicles play a crucial role in investigating air–sea interactions at the space and time scales of surface waves and in learning how surface waves influence Earth’s climate system. This better understanding could lead to improved forecasting capabilities of current weather and climate models. However, observations from moving vehicles present challenges in characterizing the properties of high-frequency surface waves. The platform speed and direction relative to the incoming waves cause the observed wave period to be Doppler shifted, particularly at high frequencies.

In this work, building upon past work on this topic (Kats and Spevak 1980; Drennan et al. 1994; Hanson et al. 1997; Cifuentes-Lorenzen et al. 2013; Collins et al. 2017; Amador et al. 2022) we present a general approach to correct Doppler effects in the directional wave spectrum so that computed

spectral wave properties are independent of the platform's motion. This method accounts for the full directionality in the wave field to properly map observed frequencies into the intrinsic frequency space, a reference frame free of Doppler effects that can be applied to any ASV. The significance of the spectral cutoff frequency is discussed by illustrating its dependence on the platform speed and relative angle. In particular, we show that it is crucial to consider the speed and direction of the platform relative to the waves during experimental planning if, for example, accurate characterization of the high-frequency portion of the wave spectrum is needed.

Last, we demonstrate the usefulness of this method with a unique dataset collected from instrumented Wave Gliders off the coast of Southern California which exhibits fluctuations in the spectral level of a wave spectrogram that are dependent upon the wave frequency, the platform speed, and the relative angle between wave and platform propagation directions. Using the 2D method, we show that Doppler effects are removed whereas fluctuations are still presented when using the 1D method. This illustrates that the intrinsic frequency reference frame, mapped using the 2D method, provides a coherent way to compare wave measurements from moving platforms and provide accurate measurements of directional surface waves down to short spatial scales [$O(1)$ m].

Central to this work is the published open-source code that automates the 2D method for Doppler-correcting directional wave spectra. The code is a collection of documented functions for MATLAB 2022 software which are publicly available on GitHub and Zenodo (see data availability statement and supplementary material for more details). This code provides easy-to-use functions to implement the methods discussed here to data collected from any ASV, thus enabling the scientific community to accurately observe and investigate short-wavelength surface waves.

Acknowledgments. The authors are grateful to Tom Farrar and the Upper Ocean Physics Laboratory at Woods Hole Oceanographic Institution for sharing their data with us. The authors are grateful to the crews of the R/V *Oceanus* and R/V *Beyster* for their support during the DELMAR2020 and SMODE2021 field deployments, respectively. This research was supported by ONR (Grant N00014-19-1-2635), and NASA (Grant 80NSSC19K1688).

Data availability statement. The data used for this study are available through the University of California, San Diego, library's Digital Collections at <https://doi.org/10.6075/JOC829GC> and it has been published as Colosi et al. (2023). The source code used to produce the figures can be accessed in the following GitHub repository <https://github.com/lcolosi/WaveSpectrum> as well as at <https://doi.org/10.5281/zenodo.8102880>.

APPENDIX

On the Solutions of k

For the mapping from observed to intrinsic frequency, we need to solve the deep-water surface wave dispersion

relation (5) for k . The analytic solutions of (5) are given by (6) and (8) along with a breakdown of them in Table 1. Here, two natural questions arise: Why do multiple solutions exist and what does each solution correspond to physically? More specifically, why in a following seas scenario are two waves with distinct frequencies in the stationary reference frame R observed at one frequency in the moving reference frame R' ?

To begin, consider a spectrum of waves on the sea surface that is observed from both the R and R' reference frames. Taking the same graphical approach as Peregrine (1976), we investigate the solutions of (5) for a given observed frequency and platform velocity by considering the intersection of the plane

$$m = \omega - \mathbf{k} \cdot \mathbf{u}, \quad (\text{A1})$$

with the surface of revolution

$$m = \pm \sigma(\mathbf{k}), \quad (\text{A2})$$

in (\mathbf{k}, m) space where ω and σ are observed and intrinsic radian frequency, respectively. Notice that the plane (A1) has a slope equal to the speed of the platform projected in the wave direction and an intercept with the m axis equal to ω . Figure A1a displays surfaces (A1) and (A2) with $\omega = 3.1412 \text{ rad s}^{-1}$, $U = 0.55 \text{ m s}^{-1}$, and $\phi = 0^\circ$. In the context of the wavenumber space in Fig. A1, the wave-number vector is defined as $\mathbf{k} = (k, l)$ using the going toward directional convention. The trace of surfaces (A1) and (A2) along the vertical planes $l = 0$ and $k = 0$ are shown in Figs. A1b and A1c, respectively. From Fig. A1, we see that multiple solutions exist due to the curvature of the dispersion relationship or the dispersive nature of deep-water surface gravity waves. That is, the nonlinearity of the dispersion relation surface (A2) and thus a frequency-dependent group and phase speed allows there to be multiple intersection points with the plane (A1). At these intersections lie our solutions for k . For nondispersive waves or waves observed from a stationary platform, multiple solutions would not exist.

Four solution points found at the intersections between traces in the $l = 0$ plane are labeled in Fig. A1b using the variables defined in Table 1. Note that the wavenumber components k and l are equal to plus or minus the wavenumber magnitude in the $l = 0$ and $k = 0$ planes, respectively, where the sign in front of k is set by the wave direction. The $l = 0$ plane corresponds to $\theta_r = 0^\circ$ and 180° , and the $k = 0$ plane corresponds to $\theta_r = 90^\circ$ and 270° .

The solution k_a corresponds to a wave with a wavenumber vector \mathbf{k} in the direction opposite of platform propagation [i.e., an approaching wave with $U \cos(\theta_r) < 0$], as seen by its negative k component, so that the observed frequency ω is greater than the intrinsic frequency σ . Similarly, the solution k_l represents a wave with a wavenumber vector \mathbf{k} in the direction of platform propagation [i.e., $U \cos(\theta_r) > 0$] so that ω is less than σ . These demonstrate the well-known Doppler effect; the next two solutions for k do not exist in the absence of platform velocity or for nondispersive waves.

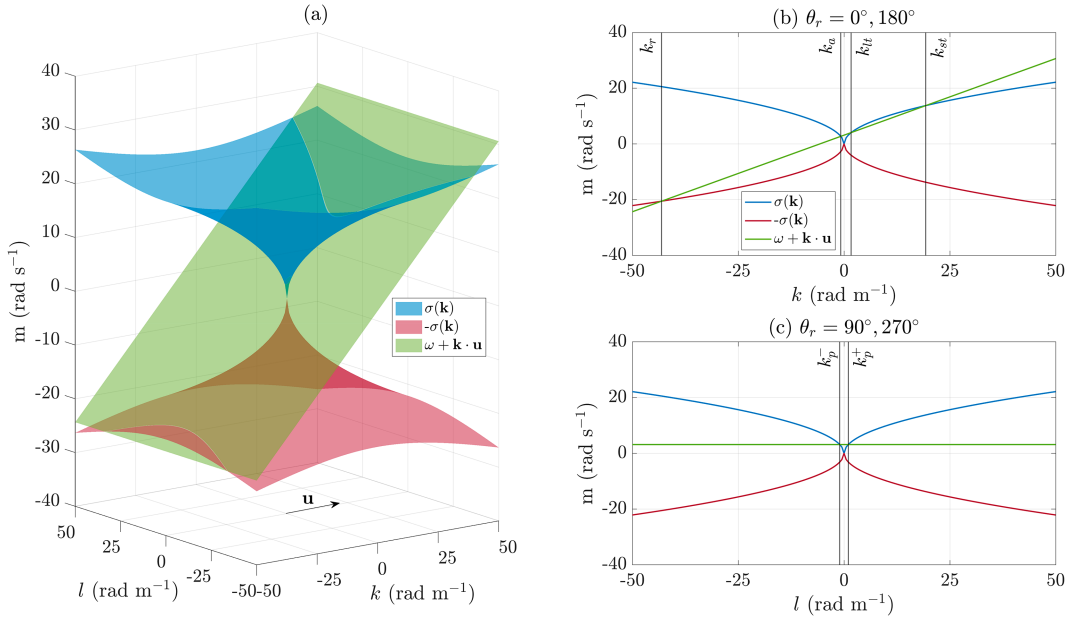


FIG. A1. (a) An illustration of the surface of revolution A2 [blue ($+\sigma$) and red ($-\sigma$) surfaces] and the plane A1 (green surface) with $\omega = 3.1412 \text{ rad s}^{-1}$, $U = 0.55 \text{ m s}^{-1}$, and $\phi = 0^\circ$. (b),(c) Values of A2 and A1 on the surfaces of constant wavenumber for $l=0$ and $k=0$, respectively. The k solutions of the dispersion relation, using variables defined in Table 1, are at intersection points of A2 and A1 (shown as the vertical black lines). The platform's velocity vector \mathbf{U} is shown in the \mathbf{k} plane.

Much like k_{lt} , the solution k_{st} corresponds to a wave propagating in the same direction as the platform. However, its crests move faster than and overtake the platform while its energy moves slower and is outran. This can be seen by looking at the slope of (A2) at the intersection point. By inspection, the slope of (A2) (i.e., the group velocity), evaluated with the intrinsic frequency associated with the intersection, is less than the slope of (A1) (i.e., the projected platform speed). However, the slope of the plane is not so great that it is twice the group velocity (i.e., the phase speed). Therefore, we arrive at $c_g < U \cos(\theta_r) < c$, which is consistent with the projected speed domain for k_{st} in Table 1. A similar argument can be made for the k_{lt} solution showing that the slope of the dispersion relation at the intersection point is greater than the plane's slope. That is, $0 < U \cos(\theta_r) < c_g$ thus corroborating the projected speed domain for k_{lt} in Table 1. k_{lt} corresponds to longer-wavelength waves with higher group and phase speeds compared to the short-wavelength waves represented by k_{st} . However, both long- and short-wavelength solutions correspond to waves with phase speed overtaking the platform. The intrinsic frequency σ associated with k_{st} is greater than the observed frequency ω more so than in the scenario for k_{lt} because the magnitude of the Doppler shift in frequency increases with wavenumber magnitude.

In Fig. A1b, the trace of plane (A1) forms a secant line to the surface (A2) for positive k . As we consider higher observed frequencies in the R' reference frame for the same speed U , we translate the trace of plane (A1) up the

m axis and the resulting secant lines approach a tangent line where $c_g = U \cos(\theta_r)$. At a sufficiently large ω , given by (10), the solutions k_{lt} and k_{st} coalesce. This transition from secant to tangent line corresponds to the bifurcation point in our solutions for k . At the bifurcation point, the wave energy is stationary relative to the platform's velocity while the wave crests will be progressing forward ahead of the platform.

The solution k_r corresponds to a wave propagating in the direction of the platform velocity but whose crests are overrun by the platform [i.e., $c < U \cos(\theta_r)$]. This causes the waves to have negative observed frequencies ($\omega < 0$) and appear to move in the opposite direction of the platform, hence the intersection with the $-\sigma$ surface and the negative wavenumber component k . Note that in reference frame R , the intrinsic frequency is in fact positive as shown in Fig. 3.

Two solution points found at the intersections between traces in the $k=0$ plane are labeled in Fig. A1c. The superscript in k_p denotes the sign of the wavenumber magnitude where $-$ and $+$ signs correspond to waves propagating in directions $\theta_r = 270^\circ$ and 90° , respectively. Solutions k_p^- and k_p^+ represent waves propagating perpendicular to the heading of the platform. This causes their projected speed in the direction of wave propagation to vanish [i.e., $U \cos(\theta_r) = 0$] and as a result, their frequencies to not be Doppler shifted.

When the platform is approaching or moving perpendicular to the waves, k is determined uniquely. However, in the case of following seas (i.e., $0^\circ \leq \theta_r < 90^\circ$ and $270^\circ \leq \theta_r < 360^\circ$),

multiple solutions for k exist leading to the frequency ambiguity. To resolve this, we need to pick one of the two possible solutions: k_{lt} or k_{st} . We make this choice using the Newton–Raphson root-finding (NRRF) algorithm, an iterative process that solves for the roots of a given real-valued function using the function's first derivative and a carefully selected initial guess (Verbeke and Cools 1995). We use the solution for k in the absence of platform forward motion (k_p) as the initial guess. Here, we recognize that at some point in time, the platform is at a state of rest on the ocean surface with $U = 0$ and observed frequencies fall along the dispersion relation given by (1) such that $\omega = \sigma(\mathbf{k})$. From this rest state, the platform speed projected onto the wave direction $U \cos(\theta_r)$ is perturbed continuously as the magnitude and direction of the platform velocity fluctuate. This, in turn, leads to continuous deformation from the dispersion relation in reference frame R , i.e., $\sigma(\mathbf{k})$, to the dispersion relation in reference frame R' , i.e., $\omega(\mathbf{k})$. Therefore, beginning with k_p will lead us to the proper solution for k . We find with this numerical approach that the solution of (5) is the lowest wavenumber magnitude branch k_{lt} thus providing an answer of which solution of k to pick.

REFERENCES

- Alvarez, A., 2015: Assessment of sea wave spectra using a surfaced glider. *Deep-Sea Res. I*, **102**, 135–143, <https://doi.org/10.1016/j.dsr.2015.04.015>.
- Amador, A., S. T. Merrifield, and E. J. Terrill, 2022: Assessment of atmospheric and oceanographic measurements from an autonomous surface vehicle. *J. Atmos. Oceanic Technol.*, **40**, 305–326, <https://doi.org/10.1175/JTECH-D-22-0060.1>.
- Bendat, J. S., and A. G. Piersol, 2011: *Random Data: Analysis and Measurement Procedures*. John Wiley and Sons, 640 pp.
- Bretherton, F. P., and C. J. R. Garrett, 1968: Wavetrains in inhomogeneous moving media. *Proc. Roy. Soc. London*, **302A**, 529–554, <https://doi.org/10.1098/rspa.1968.0034>.
- Brodtkorb, P. A., P. Johannesson, G. Lindgren, I. Rychlik, J. Rydén, and E. Sjö, 2000: WAFO—A MATLAB toolbox for analysis of random waves and loads. *10th Int. Offshore and Polar Engineering Conf.*, Seattle, WA, ISOPE, 343–350, <https://onepetro.org/ISOPEIOPEC/proceedings-abstract/ISOPE00/All-ISOPE00/ISOPE-I-00-264/7046>.
- Cavaleri, L., B. Fox-Kemper, and M. Hemer, 2012: Wind waves in the coupled climate system. *Bull. Amer. Meteor. Soc.*, **93**, 1651–1661, <https://doi.org/10.1175/BAMS-D-11-00170.1>.
- Charnock, H., 1955: Wind stress on a water surface. *Quart. J. Roy. Meteor. Soc.*, **81**, 639–640, <https://doi.org/10.1002/qj.49708135027>.
- Cifuentes-Lorenzen, A., J. B. Edson, C. J. Zappa, and L. Bariteau, 2013: A multisensor comparison of ocean wave frequency spectra from a research vessel during the Southern Ocean Gas Exchange experiment. *J. Atmos. Oceanic Technol.*, **30**, 2907–2925, <https://doi.org/10.1175/JTECH-D-12-00181.1>.
- Collins, C. O., III, and Coauthors, 2017: Doppler correction of wave frequency spectra measured by underway vessels. *J. Atmos. Oceanic Technol.*, **34**, 429–436, <https://doi.org/10.1175/JTECH-D-16-0138.1>.
- Colosi, L., N. Pizzo, L. Grare, N. Statom, and L. Lenain, 2023: Data from: Observations of surface gravity wave spectra from moving platforms. UC San Diego Library Digital Collections, <https://doi.org/10.6075/JOC829GC>.
- Dallolio, A., B. Agdal, A. Zolich, J. A. Alfredsen, and T. A. Johansen, 2019: Long-endurance green energy autonomous surface vehicle control architecture. *Oceans 2019 MTS/IEEE Seattle*, Seattle, WA, IEEE, <https://doi.org/10.23919/OCEANS40490.2019.8962768>.
- Drennan, W. M., M. A. Donelan, N. Madsen, K. B. Katsaros, E. A. Terray, and C. N. Flagg, 1994: Directional wave spectra from a swath ship at sea. *J. Atmos. Oceanic Technol.*, **11**, 1109–1116, [https://doi.org/10.1175/1520-0426\(1994\)011<1109:DWSFAS>2.0.CO;2](https://doi.org/10.1175/1520-0426(1994)011<1109:DWSFAS>2.0.CO;2).
- Fairall, C. W., E. F. Bradley, J. E. Hare, A. A. Grachev, and J. B. Edson, 2003: Bulk parameterization of air–sea fluxes: Updates and verification for the COARE algorithm. *J. Climate*, **16**, 571–591, [https://doi.org/10.1175/1520-0442\(2003\)016<0571:BPOASF>2.0.CO;2](https://doi.org/10.1175/1520-0442(2003)016<0571:BPOASF>2.0.CO;2).
- Farrar, J. T., and Coauthors, 2020: S-MODE: The Sub-Mesoscale Ocean Dynamics Experiment. *IEEE Int. Geoscience and Remote Sensing Symp.*, Waikoloa, HI, IEEE, 3533–3536, <https://doi.org/10.1109/IGARSS39084.2020.9323112>.
- Gentemann, C. L., and Coauthors, 2020: Saildrone: Adaptively sampling the marine environment. *Bull. Amer. Meteor. Soc.*, **101**, E744–E762, <https://doi.org/10.1175/BAMS-D-19-0015.1>.
- Grare, L., N. M. Statom, N. Pizzo, and L. Lenain, 2021: Instrumented wave gliders for air–sea interaction and upper ocean research. *Front. Mar. Sci.*, **8**, 664728, <https://doi.org/10.3389/fmars.2021.664728>.
- Hanson, K. A., T. Hara, E. J. Bock, and A. B. Karachintsev, 1997: Estimation of directional surface wave spectra from a towed research catamaran. *J. Atmos. Oceanic Technol.*, **14**, 1467–1482, [https://doi.org/10.1175/1520-0426\(1997\)014<1467:EODSWS>2.0.CO;2](https://doi.org/10.1175/1520-0426(1997)014<1467:EODSWS>2.0.CO;2).
- Hodges, B., L. Lenain, T. Farrar, L. Grare, K. Matsuyoshi, N. Pizzo, and N. Statom, 2023: Evaluation of ocean currents observed from autonomous surface vehicles. *J. Atmos. Oceanic Technol.*, <https://doi.org/10.1175/JTECH-D-23-0066.1>.
- Kats, A., and I. Spevak, 1980: Reconstruction of the sea-wave spectra from measurements of moving sensors. *Izv. Acad. Sci. USSR, Atmos. Oceanic Phys.*, **16**, 194–200.
- Lenain, L., and W. K. Melville, 2014: Autonomous surface vehicle measurements of the ocean's response to Tropical Cyclone Freda. *J. Atmos. Oceanic Technol.*, **31**, 2169–2190, <https://doi.org/10.1175/JTECH-D-14-00012.1>.
- , and N. Pizzo, 2020: The contribution of high-frequency wind-generated surface waves to the Stokes drift. *J. Phys. Oceanogr.*, **50**, 3455–3465, <https://doi.org/10.1175/JPO-D-20-0116.1>.
- Longuet-Higgins, M. S., 1986: Eulerian and Lagrangian aspects of surface waves. *J. Fluid Mech.*, **173**, 683–707, <https://doi.org/10.1017/S0022112086001325>.
- Lygre, A., and H. E. Krogstad, 1986: Maximum entropy estimation of the directional distribution in ocean wave spectra. *J. Phys. Oceanogr.*, **16**, 2052–2060, [https://doi.org/10.1175/1520-0485\(1986\)016<2052:MEEOTD>2.0.CO;2](https://doi.org/10.1175/1520-0485(1986)016<2052:MEEOTD>2.0.CO;2).
- McAllister, M., and T. van den Bremer, 2019: Lagrangian measurement of steep directionally spread ocean waves: Second-order motion of a wave-following measurement buoy. *J. Phys. Oceanogr.*, **49**, 3087–3108, <https://doi.org/10.1175/JPO-D-19-0170.1>.

- Melville, W. K., 1996: The role of surface-wave breaking in air-sea interaction. *Annu. Rev. Fluid Mech.*, **28**, 279–321, <https://doi.org/10.1146/annurev.fl.28.010196.001431>.
- Mitsuyasu, H., 1985: A note on the momentum transfer from wind to waves. *J. Geophys. Res.*, **90**, 3343–3345, <https://doi.org/10.1029/JC090iC02p03343>.
- Peregrine, D., 1976: Interaction of water waves and currents. *Adv. Appl. Mech.*, **16**, 9–117, [https://doi.org/10.1016/S0065-2156\(08\)70087-5](https://doi.org/10.1016/S0065-2156(08)70087-5).
- Phillips, O. M., 1985: Spectral and statistical properties of the equilibrium range in wind-generated gravity waves. *J. Fluid Mech.*, **156**, 505–531, <https://doi.org/10.1017/S0022112085002221>.
- Thomson, J., and Coauthors, 2015: Biofouling effects on the response of a wave measurement buoy in deep water. *J. Atmos. Oceanic Technol.*, **32**, 1281–1286, <https://doi.org/10.1175/JTECH-D-15-0029.1>.
- , J. B. Girton, R. Jha, and A. Trapani, 2018: Measurements of directional wave spectra and wind stress from a Wave Glider autonomous surface vehicle. *J. Atmos. Oceanic Technol.*, **35**, 347–363, <https://doi.org/10.1175/JTECH-D-17-0091.1>.
- Verbeke, J., and R. Cools, 1995: The Newton-Raphson method. *Int. J. Math. Educ. Sci. Technol.*, **26**, 177–193, <https://doi.org/10.1080/0020739950260202>.